

# Absorbing Aerosol Index: Sensitivity analysis, application to GOME and comparison with TOMS

M. de Graaf and P. Stammes

Royal Netherlands Meteorological Institute (KNMI), De Bilt, Netherlands

O. Torres

NASA Goddard Space Flight Center, Greenbelt, Maryland, USA

R. B. A. Koelemeijer

National Institute of Public Health and the Environment (RIVM), Bilthoven, Netherlands

Received 30 June 2004; revised 23 August 2004; accepted 26 November 2004; published 14 January 2005.

[1] The Absorbing Aerosol Index (AAI) was investigated and used to analyze GOME data and compare it to TOMS data. The physical interpretation of the AAI was studied with an extensive theoretical sensitivity analysis. The dependence of the method on a number of atmospheric, surface, and aerosol properties was studied using a numerical radiative transfer model. It was found to be sensitive to absorbing aerosols with wavelength-dependent refractive indices and to elevated absorbing aerosols, both with wavelength-dependent and wavelength-independent (gray) refractive indices. It was found to be insensitive to clouds, while small size scattering aerosols yield negative values. AAIs were calculated from GOME data for the period July 1995 to December 2000 and compared to TOMS AAI data. In a part of this period, July 1995 to October 1996, no TOMS observations were available, and the GOME data can be used to supplement the TOMS data set. The GOME AAI corresponds very well with known absorbing aerosol events. It suffers from lower spatial resolution and less frequent temporal coverage as compared to TOMS, but is useful as an independent data source of global aerosol measurements.

**Citation:** de Graaf, M., P. Stammes, O. Torres, and R. B. A. Koelemeijer (2005), Absorbing Aerosol Index: Sensitivity analysis, application to GOME and comparison with TOMS, *J. Geophys. Res.*, *110*, D01201, doi:10.1029/2004JD005178.

## 1. Introduction

[2] The Absorbing Aerosol Index (AAI) indicates the presence of elevated absorbing aerosols in the troposphere. It separates the spectral contrast at two ultraviolet (UV) wavelengths caused by absorbing aerosols from that of other effects, including molecular Rayleigh scattering, surface reflection, gaseous absorption and aerosol and cloud scattering [Torres *et al.*, 1998].

[3] Traditionally, aerosol optical thickness measurements are being made using spaceborne sensors operating in the visible and infrared (IR), where multiple scattering in the atmosphere is less important than in the ultraviolet (UV) and inversion calculations are relatively simple. In the visible and near-IR the large surface albedos of many land types make retrieval of aerosols difficult over these regions. With the ongoing development of numerical radiative transfer codes and increasing computational speeds accounting for multiple scattering is no longer a problem, allowing for new techniques of aerosol measurements in the UV. Because the surface albedos of both land and ocean are

small in the UV, this wavelength range should be suitable for aerosol detection over land.

[4] The AAI has many names, most notably the residue, the spectral contrast anomaly, the absorbing aerosol index or simply aerosol index. This range of names reflects the ambiguous status of the index; physical interpretation of the index is difficult. We will adopt here the name residue ( $r$ ) for the result of equation (1) in section 2.1, which is a quantity derived from measured reflectances. The name AAI is used for the index indicating absorbing aerosols, which is derived from the residue as defined in section 3.8.

[5] The residue emerged as an error estimate in the Total Ozone Mapping Spectrometer (TOMS) ozone retrieval algorithm [Torres *et al.*, 1998]. As TOMS instruments have flown, on various platforms, from 1978 to present providing nearly daily global coverage, the TOMS AAI record is the longest aerosol record available and it is used extensively to investigate aerosol impact on climate and study heavy dust, biomass burning and volcanic eruption events [e.g., Hsu *et al.*, 1996; Herman *et al.*, 1997; Seftor *et al.*, 1997; Chiapello *et al.*, 1999; Pandithurai *et al.*, 2001; Alpert and Ganor, 2001; Moulin and Chiapello, 2004]. However, from May 1993 to June 1996 no TOMS observations were available.

[6] The purpose of this paper is twofold. Firstly, physical interpretation of the absorbing aerosol index is facilitated by presenting an extensive analysis of the main sensitivities of the index, which we feel is missing in the literature. A theoretical basis for the AAI was given by *Torres et al.* [1998], using aerosol models with spectrally independent refractive indices  $m$ . The radiance changes for different surface albedos, aerosol refractive indices, aerosol layer height and solar zenith angles were discussed, giving insight in the behavior of an aerosol laden atmosphere and the resulting residue values therein. The main sensitivities are known: the residue is dependent on aerosol type [*Torres et al.*, 1998] and aerosol single scattering albedo and aerosol layer height [*Herman et al.*, 1997], but to which extent is unclear.

[7] Recently, new evidence showed the incorrectness of the assumption of a spectrally independent refractive index for mineral dust and the implications for the AAI [*Sinyuk et al.*, 2003; *Mahowald and Dufresne*, 2004]. In the present study the sensitivity of the residue for spectrally dependent refractive indices is compared to the residues found for spectrally independent refractive indices. Other sensitivities are studied as well. The definition of the residue is given in section 2 and the calculation method used in this paper is presented. In section 3 the influence on the residue of aerosol micro- and macrophysical parameters, atmospheric optical, physical and chemical parameters and surface parameters are investigated separately, by means of a radiative transfer model study.

[8] Secondly, the current TOMS AAI record is compared to and supplemented with AAIs derived from five and a half years of Global Ozone Monitoring Experiment (GOME) data. In section 4 the GOME data are presented for the period July 1995 to December 2000, and the derived residue and AAI products are described.

## 2. Residue Method

[9] In this section, the definition and derivation of the residue is given and the method of calculation used for the GOME data. The AAI is a quantity derived from the residue. Its definition will be given after the sensitivity study of section 3.

### 2.1. Definition of the Residue

[10] The residue  $r$  is a wavelength-dependent variable defined as [*Herman et al.*, 1997]

$$r_{\lambda} = -100 \cdot \left\{ 10 \log \left( \frac{I_{\lambda}}{I_{\lambda_0}} \right)^{\text{meas}} - 10 \log \left( \frac{I_{\lambda}}{I_{\lambda_0}} \right)^{\text{Ray}} \right\}, \quad (1)$$

where  $I_{\lambda}$  is the radiance at the top of the atmosphere (TOA) at a wavelength  $\lambda$ . The superscript <sup>meas</sup> refers to a measured TOA radiance of a real atmosphere with aerosols, as opposed to a calculated TOA radiance for an aerosol-free atmosphere with only Rayleigh scattering and absorption by molecules and surface reflection and absorption. The latter is referred to as <sup>Ray</sup>.

[11] The reflectance is defined as

$$R = \frac{\pi I}{\mu_0 E_0}, \quad (2)$$

where  $E_0$  is the solar irradiance at TOA perpendicular to the direction of the incident sunlight and  $\mu_0$  is the cosine of the solar zenith angle  $\theta_0$ . So  $\mu_0 E_0$  is the solar irradiance at TOA incident on a horizontal surface unit. Using equation (2), we can replace all quotients of radiances in equation (1) with quotients of reflectances.

[12] If the surface albedo  $A_s$  for the Rayleigh atmosphere calculation is chosen so that

$$R_{\lambda_0}^{\text{meas}} = R_{\lambda_0}^{\text{Ray}}(A_s), \quad (3)$$

where  $\lambda_0$  is a reference wavelength, equation (1) can be reduced to

$$r_{\lambda} = -100 \cdot 10 \log \left( \frac{R_{\lambda}^{\text{meas}}}{R_{\lambda}^{\text{Ray}}} \right), \quad (4)$$

where  $R_{\lambda}^{\text{Ray}}$  is calculated for surface albedo  $A_s(\lambda_0)$ , so the surface albedo is assumed to be constant in the range  $[\lambda, \lambda_0]$ . In this paper we will look at several wavelength pairs  $\lambda/\lambda_0$ : 340 nm/380 nm, 331 nm/360 nm and 335 nm/380 nm.

### 2.2. Calculation of the Residue

[13] Equation (3) involves finding a surface albedo for which the measured reflectance at the reference wavelength is equal to the reflectance of a pure Rayleigh atmosphere with all scattering and absorption effects accounted for in the surface albedo. This inversion process was performed with Lookup Tables (LUTs) of the reflectances, as described below.

[14] On the assumption that the atmosphere is bounded from below by a Lambertian surface, which reflects incident radiation uniformly and unpolarized in all directions, the surface contribution to the reflectance at TOA can be separated from that of the atmosphere [*Chandrasekhar*, 1960]:

$$R(\mu, \mu_0, \phi - \phi_0, A_s) = R_0(\mu, \mu_0, \phi - \phi_0) + \frac{A_s t(\mu) t(\mu_0)}{1 - A_s s^*}. \quad (5)$$

The first term,  $R_0$ , is the path radiance, which is the atmospheric contribution to the reflectance. The second term is the contribution of the surface with an albedo  $A_s$ .  $t$  is the total atmospheric transmission,  $s^*$  is the spherical albedo of the atmosphere for illumination from below,  $\mu$  is the cosine of the viewing zenith angle  $\theta$  and  $\phi - \phi_0$  is the relative azimuth angle. The path radiance can be expanded in a Fourier series. For a Rayleigh atmosphere, when  $R = R_{\lambda_0}^{\text{Ray}}$ , the expansion is exact with only three terms in  $\phi - \phi_0$ , because of the cosine-squared scattering angle dependence:

$$R_0(\mu, \mu_0, \phi - \phi_0) = a_0 + \sum_{i=1}^2 2a_i(\mu, \mu_0) \cos i(\phi - \phi_0). \quad (6)$$

**Table 1.** Parameters for the Aerosol Models Used in This Study

Aerosol Model	Type	Size Parameters			Im( $m$ )		$\omega_0$		$g$		$\tau$	
		$r_0(\mu)$	$\sigma$	Re( $m$ )	340	380	340	380	340	380	340	380
C2	Mie	0.14	1.45	1.55	0.04	0.04	0.82	0.83	0.73	0.73	1.00	1.04
D1a	Mie	0.12	2.20	1.55	0.006	0.0042	0.90	0.93	0.70	0.69	1.00	1.01
D3	Mie	0.50	2.20	1.55	0.006	0.0042	0.75	0.81	0.83	0.80	1.00	1.01
	HG <sup>a</sup>	-	-	-	-	-	0.90	0.90	0.70	0.70	1.00	1.00

<sup>a</sup>Default values. If other values are used, it will be indicated.

$R_0$  is calculated with LUTs of  $a_i(\mu, \mu_0)$ ,  $t(\mu)$  and  $s^*$  for all wavelengths used. Then the surface albedo  $A_s$  in equation (3) can be found from

$$A_s = \frac{R - R_0}{t(\mu)t(\mu_0) + s^*(R - R_0)}, \quad (7)$$

by replacing  $R$  by  $R_{\lambda_0}^{meas}$  in equation (7). Note that this equation allows negative surface albedos, which occurs for highly absorbing (aerosol) layers.

[15] Lookup tables of  $a_i$ ,  $t(\mu)$  and  $s^*$  were prepared as a function of  $\mu$  and  $\mu_0$ , surface pressure  $P_s$  and ozone column density  $\Omega$  with the radiative transfer model DAK, described in section 3.1. The coefficients were calculated for 42 Gaussian distributed  $\mu$  and  $\mu_0$  points, ozone columns of 167 and 501 DU and surface pressures of 1013, 802, and 554 hPa, as the dependence of the residue on total ozone column was found to be linear, whereas the dependence on surface pressure was nonlinear, see section 3.6. The surface albedo and reflectance were found by interpolation between these points. Interpolation between ground pressure points was performed with a second order polynomial, all other interpolations were linear.

### 3. Residue Sensitivities

[16] The effects of several aerosol parameters on the residue were studied, as well as the effect of polarization, clouds and atmospheric constituents, using the radiative transfer model DAK. Thereto the measured reflectances ( $R_\lambda/R_{\lambda_0}$ ) were replaced by simulated reflectances. The 340 nm/380 nm pair was chosen as the default wavelength pair.

#### 3.1. Radiative Transfer Model DAK

[17] The Rayleigh atmosphere reflectances and the LUT coefficients were calculated with the Doubling-Adding KNMI (DAK) radiative transfer model [Stammes, 2001]. This model computes the monochromatic reflectance and transmittance in a plane-parallel atmosphere including polarization, using the polarized doubling-adding method [De Haan et al., 1987]. This method calculates the polarized internal radiation field of the atmosphere in an arbitrary number of layers, each of which can have Rayleigh scattering, gas absorption, and aerosol and cloud particle scattering and absorption.

#### 3.2. Standard Atmosphere, Geometry, and Definition of Aerosol Models

[18] For the atmospheric gas and temperature profile the standard Mid-Latitude Summer (MLS) atmosphere [Anderson et al., 1986] was adopted throughout all calcu-

lations. The standard ground pressure was 1013 hPa, the standard ozone column was 334 DU. Linear polarization was taken into account. A surface albedo of 0.05 was used to simulate dark surfaces and 0.6 to simulate bright surfaces. An aerosol layer could be introduced to simulate aerosol effects. The default altitude of the bottom of this 1 km thick layer was 3 km.

[19] Two different types of phase functions were used to simulate the aerosols: the Henyey-Greenstein (HG) and Mie phase functions. The HG phase function is defined as [Henyey and Greenstein, 1941]

$$\Phi(\cos \Theta) = \frac{1 - g^2}{(1 + g^2 - 2g \cos \Theta)^{3/2}}. \quad (8)$$

Here  $\Theta$  is the scattering angle and  $g = \langle \cos \Theta \rangle$  is the asymmetry parameter. The asymmetry parameter is a measure for the amount of forward scattered radiation by aerosols; the greater  $g$ , the greater the amount of radiation scattered in the forward direction. For Rayleigh scattering the amount of radiation in the forward direction is equal to the amount of backward scattering, so  $g$  is zero. The default value for the asymmetry parameter chosen for HG aerosol was  $g = 0.7$ , representing moderately forward scattering aerosols. The analytic HG function can be used to separate the effects of the single scattering albedo and the asymmetry parameter.

[20] Mie aerosol phase functions were used to model more realistic aerosols. In Mie calculations the complex refractive index  $m$  needs to be changed to vary the single scattering albedo, which also affects the asymmetry parameter. This introduces spectral variations in these parameters, which affect the residue calculations. Three types of aerosols were used, a carbonaceous aerosol model (C2), a small mode dust aerosol model (D1a) and a large mode dust aerosol model (D3). C2 is a smoke model with wavelength-independent refractive index defined in Torres et al. [1998], D1a is the fine dust model introduced in Torres et al. [2002], with the updated imaginary part of the refractive index of Sinyuk et al. [2003]. D3 is the large mode dust aerosol model as defined by Torres et al. [1998], also with the updated imaginary part of the refractive index of Sinyuk et al. [2003]. In Table 1 the values of the parameters of the different aerosol models used in this study are summarized. The size distribution of the Mie aerosols was assumed to be lognormal.

[21] The default viewing zenith angle  $\theta$  in all sensitivity runs was zero (nadir view) and the default solar zenith angles  $\theta_0$  were  $0^\circ$ ,  $15^\circ$ ,  $30^\circ$ ,  $45^\circ$  (and  $60^\circ$ ). The values of the residue increase quickly for solar zenith angles  $\theta_0$  and viewing zenith angles  $\theta$  larger than  $60^\circ$ , see Figures 1a–1c. The relative azimuth angle ( $\phi - \phi_0$ ) is  $0^\circ$ ,  $90^\circ$  and  $180^\circ$  in these figures, respectively. Because the radiative transfer code is plane



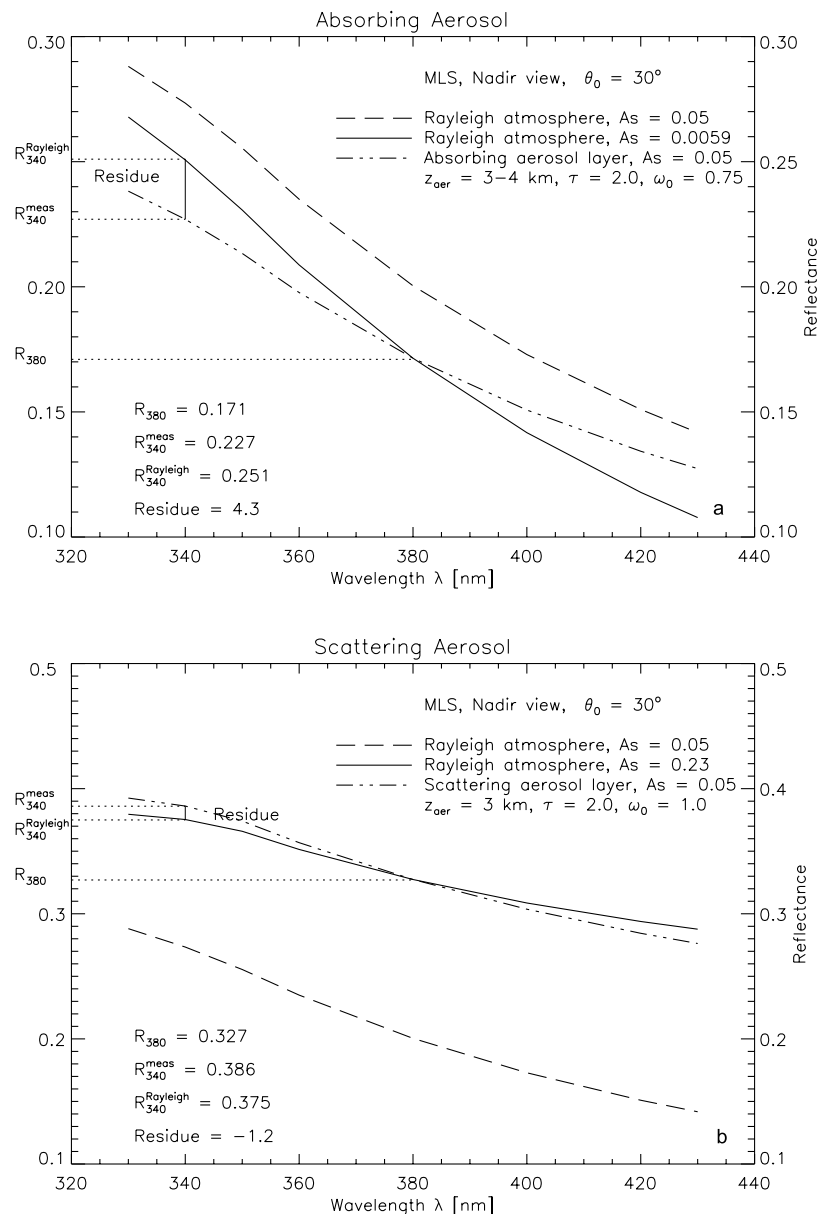


**Figure 2.** The 340 nm/380 nm residue calculation in an atmosphere with (a) absorbing aerosols and (b) scattering aerosols. Solar zenith angle  $\theta_0$  is  $30^\circ$ ; viewing zenith angle  $\theta$  is  $0^\circ$ . Aerosols are present between 3 and 4 km, with optical thickness  $\tau$  is 2.0, the aerosol single scattering albedo  $\omega_0$  is 0.75 for absorbing aerosols (Figure 2a) and 1.0 for scattering aerosols (Figure 2b). The phase function of the aerosols is modeled with a Henyey-Greenstein function with an asymmetry parameter of 0.7. See text for explanation of the plots.

*Panel on Climate Change (IPCC), 2001].* In this range the residue is raised for stronger forward scattering (Figure 3b). For higher  $g$  the effect of scattering is reduced compared to the effect of absorption, leading to higher residues. Also, as the amount of forward scattered radiation increases, more radiation reaches the surface where absorption takes place yielding a higher residue. This was confirmed in a run with high surface albedo (0.6), where the increase of residue with increasing  $g$  was much less than for a low surface albedo (0.05).

[29] Aerosol optical thickness: The residue increases with increasing optical thickness  $\tau$  (Figure 4a). The residue is zero for zero optical thickness by definition. As the optical

thickness increases Rayleigh scattering is suppressed and more radiation is absorbed. Therefore less radiation will emerge at TOA and the deviation from the clear sky radiation increases, yielding a higher residue. This is the basis for the detection of absorbing aerosols. A linear increase of residue with optical thickness with a slope proportional to the single-scattering albedo was also found by Torres *et al.* [1998] and Herman *et al.* [1997].

[30] Aerosol layer altitude: The residue is highly dependent on the altitude  $z$  of the aerosol layer (Figure 4b; the value on the x axis in this figure refers to the base of the 1 km thick aerosol layer). The dependence is nearly linear in height, as was found by Torres *et al.* [1998] and

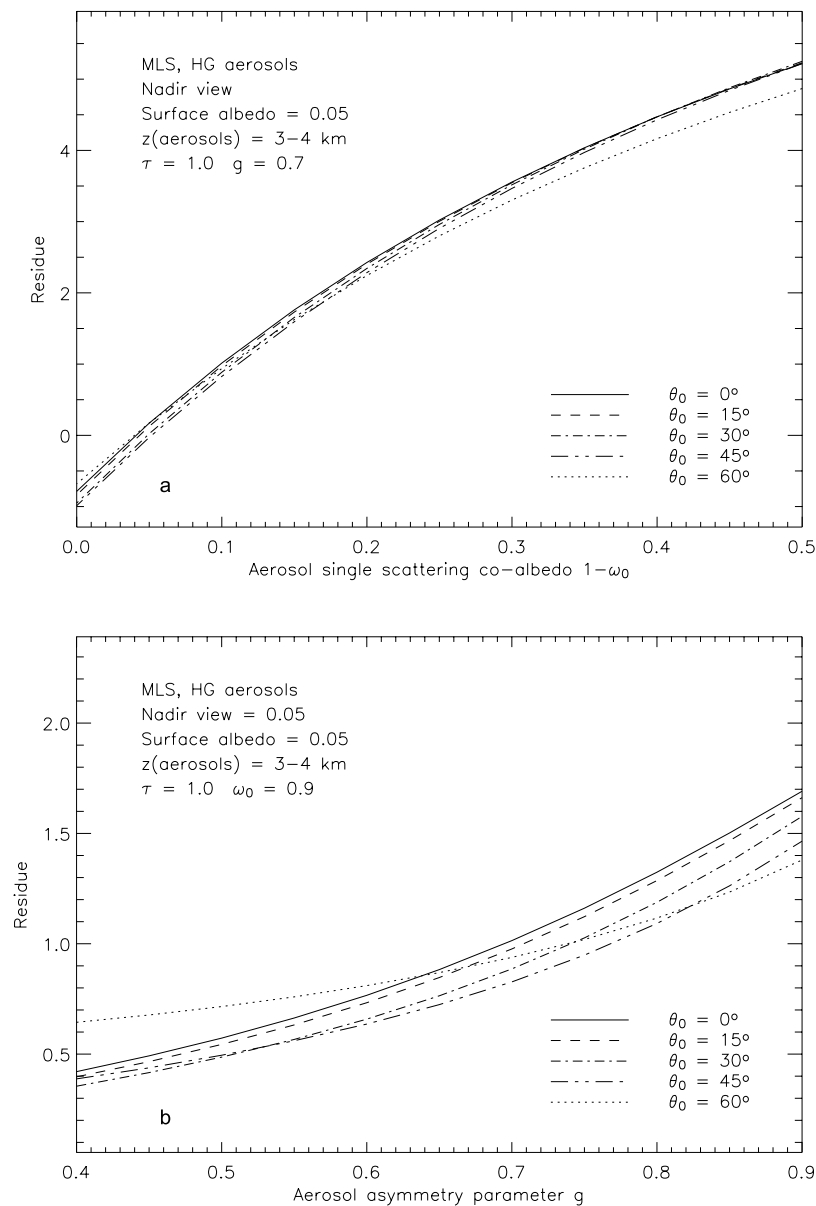


**Figure 3.** HG aerosols: (a) Dependence of the residue on aerosol single scattering co-albedo  $1 - \omega_0$ . (b) Dependence of the residue on aerosol asymmetry parameter  $g$ .

Herman *et al.* [1997]. Absorbing aerosols mainly interact with Rayleigh scattered radiation coming from below the aerosol layer. The higher the aerosol layer, the greater the amount of affected Rayleigh scattered radiation, increasing the residue. This means that the residue method is especially suited for detection of elevated tropospheric aerosols and stratospheric aerosols.

### 3.5. Sensitivity of the Residue for Mie Aerosol

[31] Data on aerosol properties suggest that the refractive index of dust aerosol is strongly wavelength-dependent in the UV [Patterson *et al.*, 1977; Sinyuk *et al.*, 2003]. This has implications for the residue, as will be shown below with the Mie aerosol models, in which this wavelength dependence is taken into account.

[32] Aerosol optical thickness: Like with HG aerosol, the residue increases with aerosol optical thickness

(Figure 5a). The increase is larger for larger aerosols, because the single scattering albedo is smaller (see Table 1). The residue is also much larger for aerosols with a wavelength-dependent refractive index than for gray aerosols (compare Figures 4a and 5a); although the D1a aerosols have almost the same characteristics as the HG aerosols, they produce a much stronger residue increase for increasing aerosol optical thickness than the HG aerosols.

[33] Aerosol layer altitude: The residue increases linearly with aerosol layer altitude, like it did for HG aerosol (compare Figures 4b and 5b). The slope is proportional to the aerosol single scattering co-albedo, as was found in previous studies [Herman *et al.*, 1997; Torres *et al.*, 1998]. However, there is an off-set for aerosols with a wavelength-dependent refractive index: using gray aerosols the residue is positive only for aerosol higher

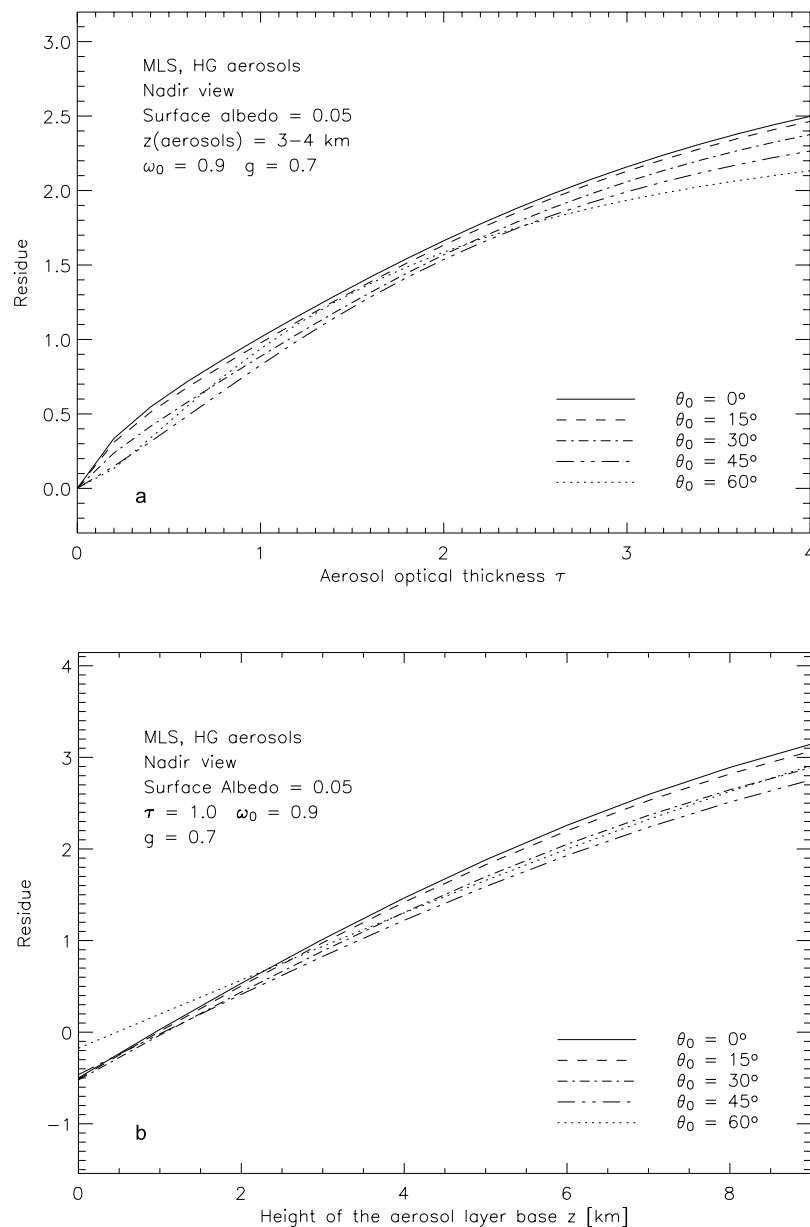


**Figure 4.** HG aerosols: (a) Dependence of the residue on aerosol optical thickness  $\tau$ . (b) Dependence of the residue on altitude of the aerosol layer  $z$ .

than about 1 to 2 km in altitude, whereas nongray absorbing aerosols can be detected even very close to the surface.

[34] This result is consistent with the study of *Mahowald and Dufresne* [2004], who found a stronger residue signal over mineral aerosol sources when gray dust aerosol models were replaced by aerosol models with wavelength-dependent refractive indices. This implied the detection of nongray aerosols closer to the surface, and thus closer to the source, than previously assumed.

### 3.6. Sensitivity of the Residue to Atmospheric and Surface Parameters

[35] Surface albedo: Increasing the surface albedo has two competing effects. Firstly, it will increase the role of absorption by the aerosol layer compared to that of the surface. The reason is that below the aerosol layer radiation

is bounced back and forth between the surface and the aerosol layer before escaping to space. Absorption takes place each time both at the surface and in the aerosol layer. When the surface albedo is raised, the relative importance of the absorption by aerosols is increased, amplifying the effect of the absorption characteristics of the aerosol layer. This can be spectrally flat, producing no effect on the residue with increasing surface reflection, or wavelength-dependent, increasing the residue with increasing surface reflection.

[36] Secondly, increasing the surface albedo increases the amount of directly reflected radiation emerging at the top of the atmosphere, which results in itself in a zero residue. This will reduce the effect of an aerosol layer and lower the residue for increasing surface reflection.

[37] For aerosols of type D1a and D3, with strongly wavelength-dependent single scattering albedo, the first

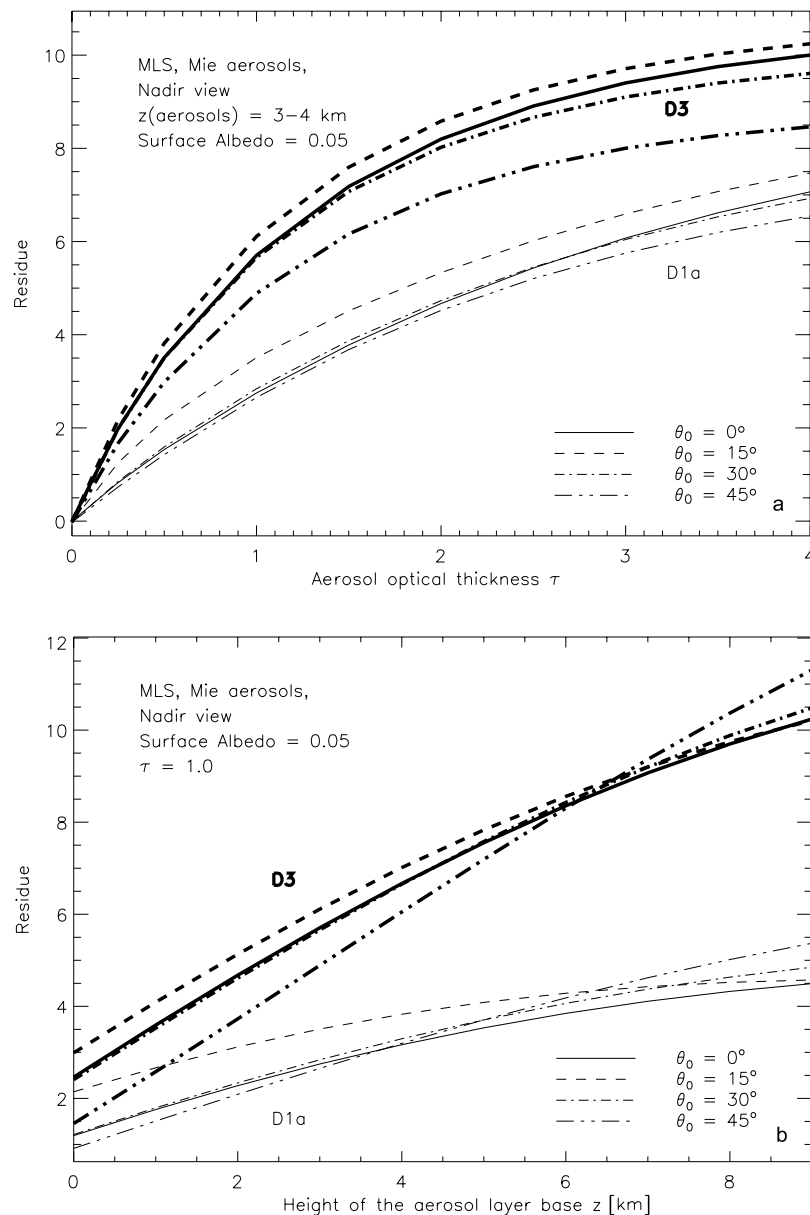


**Figure 5.** Mie aerosols: (a) Dependence of the residue on aerosol optical thickness  $\tau$ . (b) Dependence of the residue on altitude of the aerosol layer  $z$ .

effect is most important. So the residue increases for increasing surface reflection (Figure 6a).

[38] For HG aerosols, with wavelength-independent single scattering albedo, the first effect results in a constant residue for increasing surface albedo, but the second effect reduces the residue (Figure 6b). This is also true for a thin aerosol (gray or nongray) layer; the presence of such a layer will only be felt when the amount of directly reflected radiation by the surface is small. On the other hand, the residue of a very thick layer of gray aerosols is constant with increasing surface albedo (not shown).

[39] For smoke aerosols, like the C2 model with a weakly wavelength-dependent single scattering albedo, the two effects balance each other, and the residue does not change much with increasing surface albedo (Figure 6b).

[40] The above result for gray absorbers can also be found in *Torres et al.* [1998], where the residue versus

aerosol optical thickness was modeled using gray absorbing and scattering aerosols over a dark ( $A_s = 0.05$ ) and a bright surface ( $A_s = 0.6$ ). Using a bright surface instead of a dark surface hardly changed the residue for the absorbing aerosols [*Torres et al.*, 1998, Figure 5]. The above result for the nongray aerosols seems to be confirmed by observations. TOMS AAI values are larger over underlying clouds, which serve as a bright surface. Smoke aerosols have been observed over both dark surfaces (e.g., biomass burning aerosols over tropical forests in South America [*Gleason et al.*, 1998]) and over bright surfaces (e.g., biomass burning aerosols over snow and ice in Greenland [*Hsu et al.*, 1999]).

[41] Clouds: The effect of clouds on the residue is comparable to the effect of a high surface albedo when the aerosols overlie the cloud. However, when the cloud overlies the aerosols the residue is completely determined

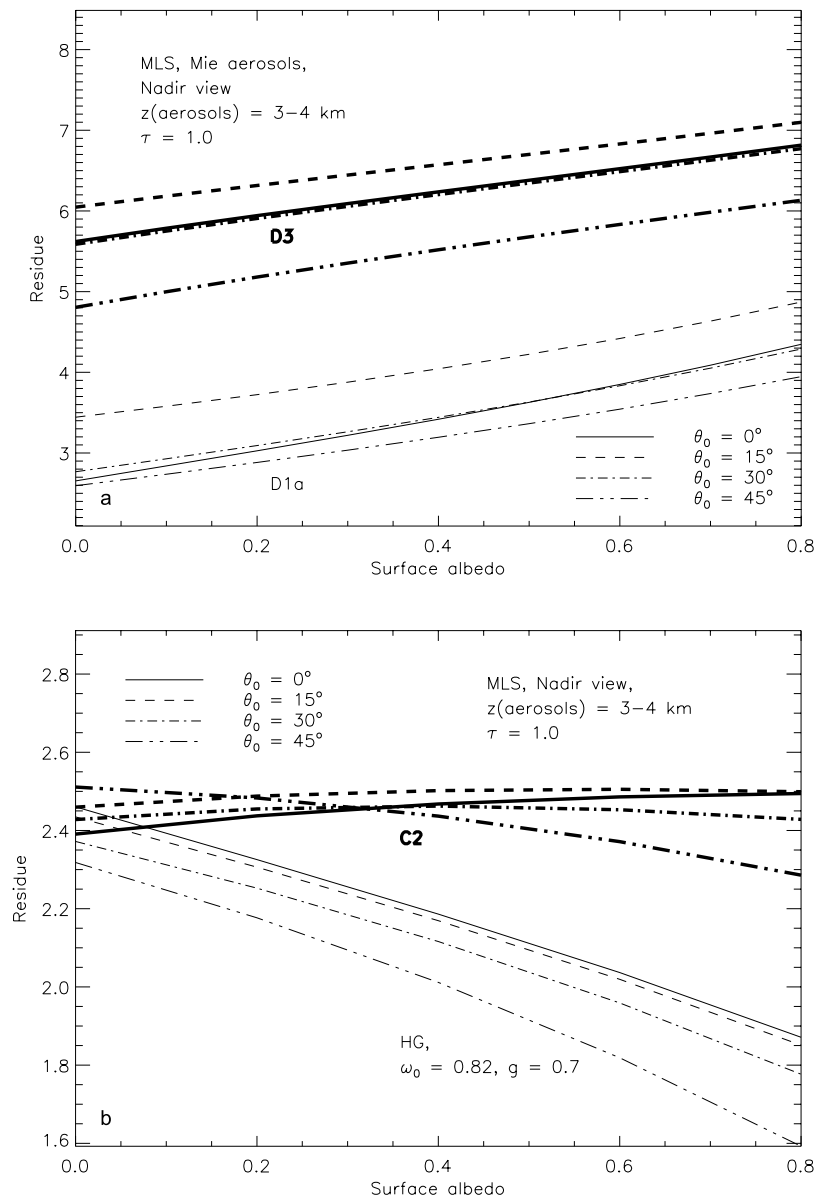


**Figure 6.** Dependence of the residue on surface albedo for nadir view and solar zenith angles between  $0^\circ$  and  $45^\circ$ . (a) Atmosphere with Mie aerosols type D1a (normal lines) and D3 (bold lines). (b) Atmosphere with Mie aerosols type C2 (bold lines) and HG aerosols with C2 characteristics:  $\tau = 1.0$ ,  $\omega_0 = 0.82$ ,  $g = 0.7$  (normal lines).

by the cloud characteristics. This is illustrated in Figure 7a with HG aerosols (the effect for Mie aerosols can be inferred from Figure 6). In Figure 7a a cloud was present at different altitudes in an atmosphere with an absorbing HG aerosol layer at an altitude of 3–4 km. The cloud is modeled as scattering HG aerosols characterized by a high optical thickness of  $\tau = 50$ , an asymmetry parameter  $g = 0.85$  and a single scattering albedo  $\omega_0 = 1.0$ . The vertical extent of the cloud is 1 km.

[42] When the cloud is present under the aerosol layer (left side of Figure 7a), the residue is the same as for an aerosol layer over a bright surface. The cloud reflects almost all light incident on it, so effectively it becomes the new surface. As the cloud base is raised from 0 to 3 km the residue is slightly reduced due to a decrease in

the amount of intercepted radiation by the aerosol layer (the distance between the cloud and the aerosol layer is reduced). Then there is a transition to a new situation when the cloud base is between 3 and 4 km and coincides with the aerosol layer. The residue drops by about 0.9. When the cloud base is raised even further the residue stays almost constant. The cloud intercepts almost all incident radiation and acts as an opaque “roof” over the aerosol layer; consequently, the residue is almost entirely determined by the cloud characteristics. Cloud droplets are in fact scattering aerosols and produce zero or negative residues, depending on the solar zenith angle. This means that the residue method will not be affected very much by low clouds, but high clouds will certainly obscure absorbing aerosols layers.

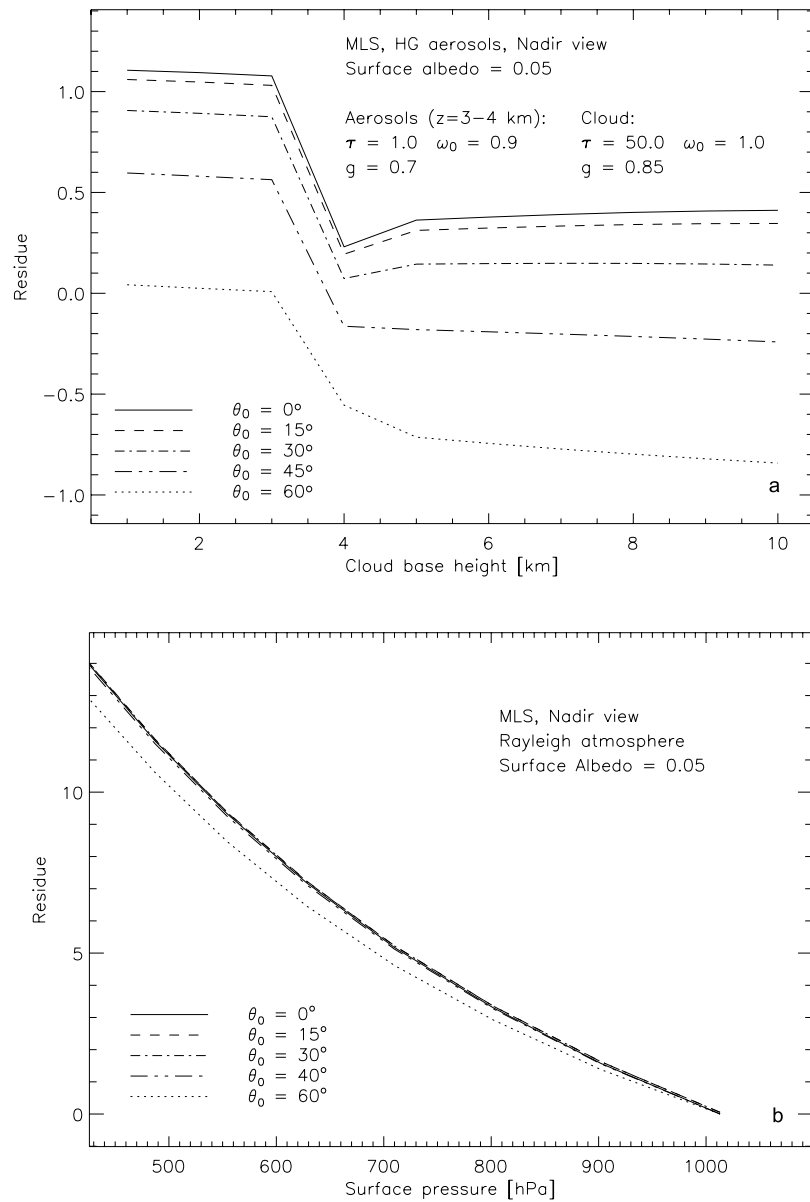


**Figure 7.** (a) Dependence of the residue on cloud base height, with an aerosol layer between 3 and 4 km altitude. The cloud has optical thickness  $\tau = 50.0$  and scattering particles with  $\omega_0 = 1.0$  and  $g = 0.85$ . The base of the 1 km thick cloud was varied between 0 and 10 km in steps of 1 km. (b) Dependence of the residue on surface pressure. Rayleigh atmosphere with MLS profile, nadir view, solar zenith angles vary between  $0^\circ$  and  $60^\circ$ .

[43] Ozone absorption: A linear relationship between residue and ozone was found by scaling the total ozone column  $\Omega$  (not shown). The reduction of the TOA radiance due to ozone absorption is, to first order, equal to  $\exp(-\tau_{O_3}M)$ , where  $\tau_{O_3}$  is the optical thickness of the ozone column and  $M$  is the geometrical airmass factor,  $M = 1/\mu_0 + 1/\mu$ . Since  $\tau_{O_3}$  is about 0.01 at 340 nm, the exponential can be approximated by  $1 - \tau_{O_3}$ .

[44] The dependence of the residue on  $\Omega$  is limited: if  $\Omega$  is increased from 100 to 500 DU, the 340 nm/380 nm residue increases by 1, for the 335 nm/380 nm residue the increase is twice as large, but still linear. Therefore the ozone contribution in a Rayleigh atmosphere can be corrected for by linear interpolation. The LUTs include this dependence on  $\Omega$  (see section 2.2).

[45] Regarding the interaction of the absorption processes by ozone and aerosols, it has been shown that particle absorption effects introduce errors in the TOMS total ozone retrieval process, and a correction method making use of AAI has been developed [Torres and Barthia, 1999].

[46] Surface pressure: The residue is strongly dependent on surface pressure (Figure 7b). The surface pressure was lowered by removing the lower part of a Rayleigh atmosphere, which also simulates the effect of topography. In this way an apparent residue is introduced, as a result of the reduced multiple scattering due to the lower amount of Rayleigh scatterers in the atmosphere. This effect is wavelength-dependent, with more multiple scattering at lower wavelengths, yielding a residue. The dependence is not linear (Figure 7b), therefore the surface pressure is

**Table 2.** Wavelengths Used to Calculate a Residue From Various UV Satellite Instruments

Instrument	Platform	Period	$\lambda$ /nm	$\lambda_0$ /nm
TOMS	Nimbus-7	1978–1993	340	380
TOMS	METEOR-3	1991–1994	340	380
TOMS	ADEOS	1996–1997	340	380
TOMS	Earth Probe	1996 to present	331	360
GOME	ERS-2	1995 to present	335	380

accounted for by a second order polynomial interpolation in the residue calculations (see section 2.2).

### 3.7. Sensitivity of the Residue to Other Optical Parameters

[47] Wavelength: The wavelength pair ( $\lambda$ ,  $\lambda_0$ ) in equation (1) determines the absolute value of the residue. In the next sections residues from various satellite instruments will be presented. Most of these instruments use different wavelength pairs (Table 2); therefore the effect of varying the wavelengths was investigated.

[48] Firstly, the 340 nm/380 nm residue, as used for the first three TOMS instruments, was compared to the 335 nm/380 nm residue, used for GOME, for varying geometries, surface reflectances, aerosol characteristics and aerosol layer heights, 83,160 configurations in total. The residue is increased by about 10% when the radiance at 335 nm is used instead of the radiance at 340 nm for all cases (Figure 8a). This is expected for a wavelength pair lying farther apart; at 335 nm multiple Rayleigh scattering is more important, increasing the optical path through the absorbing aerosol layer and increasing the chance of absorption. It can also be seen from Figure 2a.

[49] Secondly, the 331 nm/360 nm residue, used for the latest TOMS instrument, was compared to the 335 nm/380 nm residue (Figure 8b). The 331 nm/360 nm residues are about 35% smaller than the 335 nm/380 nm residues. The relationship now becomes nonlinear because of the use of different reference wavelengths  $\lambda_0$ . The second, smaller branch in Figure 8b is caused by highly absorbing aerosols ( $\omega_0 = 0.6–0.7$ ) over a dark surface ( $A_s = 0.05$ ). For these points large negative surface albedos are needed for the equivalent Rayleigh curves. This causes nonphysical effects to play a role in the calculations and breaks down the linearity. Because of the larger Rayleigh optical thickness at 360 nm than at 380 nm this effect is greater for the 331 nm/360 nm residue than for the 335 nm/380 nm residue.

[50] The difference between the 331 nm/360 nm and 340 nm/380 nm residues was also checked and showed a similar pattern as shown in Figure 8b, but the mean difference was now 25%, as expected.

[51] Polarization: Inclusion of polarization is essential in Rayleigh multiple scattering calculations in the UV. When (linear) polarization was not accounted for in the LUTs calculations, errors in the reflectances yielded residues as large as 4 to 5 in pure Rayleigh atmospheres (where residues need to be zero by definition).

### 3.8. Conclusion; Defining the Absorbing Aerosol Index

[52] The above sensitivity study shows that there are at least two possibilities to create a positive residue. Firstly, an absorbing aerosol layer can absorb Rayleigh scattered

radiation from below the layer. Because the Rayleigh optical thickness is strongly wavelength-dependent, this creates a difference in the reflectance at two UV wavelengths relative to that of a Rayleigh atmosphere, even with gray absorbers. When the absorbing ability of the layer increases more radiation is absorbed and the deviation increases, increasing the residue. The same is true when the amount of atmosphere under the absorbing layer increases.

[53] Secondly, the aerosol absorption itself can be wavelength-dependent, creating a spectral difference in the TOA reflected radiation. This will also create a positive residue if the absorption at the shorter wavelength is stronger, even when the aerosol layer is close to the surface. When the spectral absorption difference increases the residue will increase, meaning that different aerosol types produce different residues under the same circumstances.

[54] For an atmosphere which is dominated by scattering (either by particles, molecules, the surface or clouds) the reflectance will not deviate much from the reflectance of a Rayleigh atmosphere with an adjusted surface albedo, yielding zero or small negative residues.

[55] Therefore the AAI is defined only when a positive residue is found, which excludes clouds and scattering aerosols. The calculation often involves using negative surface albedos, and its absolute value has no unique interpretation, but high values of the AAI indicate the presence of absorbing aerosol layers, both over dark and bright surfaces. There have been some efforts of translating the AAI into physical meaningful parameters [Gleason *et al.*, 1998; Hsu *et al.*, 1999], but we prefer to present the AAI itself rather than a derived product, because the interpretation of the AAI is still developing.

[56] The next sections show that the AAI corresponds well to occurrences of biomass burning and dust events, which are major sources of absorbing aerosols.

## 4. AAI From GOME and TOMS

[57] AAIs were retrieved from Global Ozone Monitoring Experiment (GOME) data and compared to the AAIs derived from various Total Ozone Mapping Spectrometers (TOMS) instruments that have flown for the past 24 years. AAI data were derived from GOME before for the SCAR-B study [Gleason *et al.*, 1998], but only two weeks of data of GOME in its validation phase were considered. GOME data have also been used to retrieve aerosol optical thickness information [Torricella *et al.*, 1999], but these data are not very reliable. This is probably due to cloud contamination in the data.

### 4.1. TOMS

[58] The Total Ozone Mapping Spectrometers (TOMS) were designed to provide daily global maps of ozone. Four TOMS instruments have flown on different platforms to provide a long term record of global ozone maps and related data products, among which is the AAI. Nimbus-7/TOMS was the most successful instrument, operating for fourteen years, from October 1978 to May 1993. Meteor-3/TOMS flew from October 1991 until December 1994. ADEOS/TOMS was launched in August 1996 after an eighteen month period when the program had no on-orbit capability and provided data until June 1997. Earth Probe (EP)/TOMS

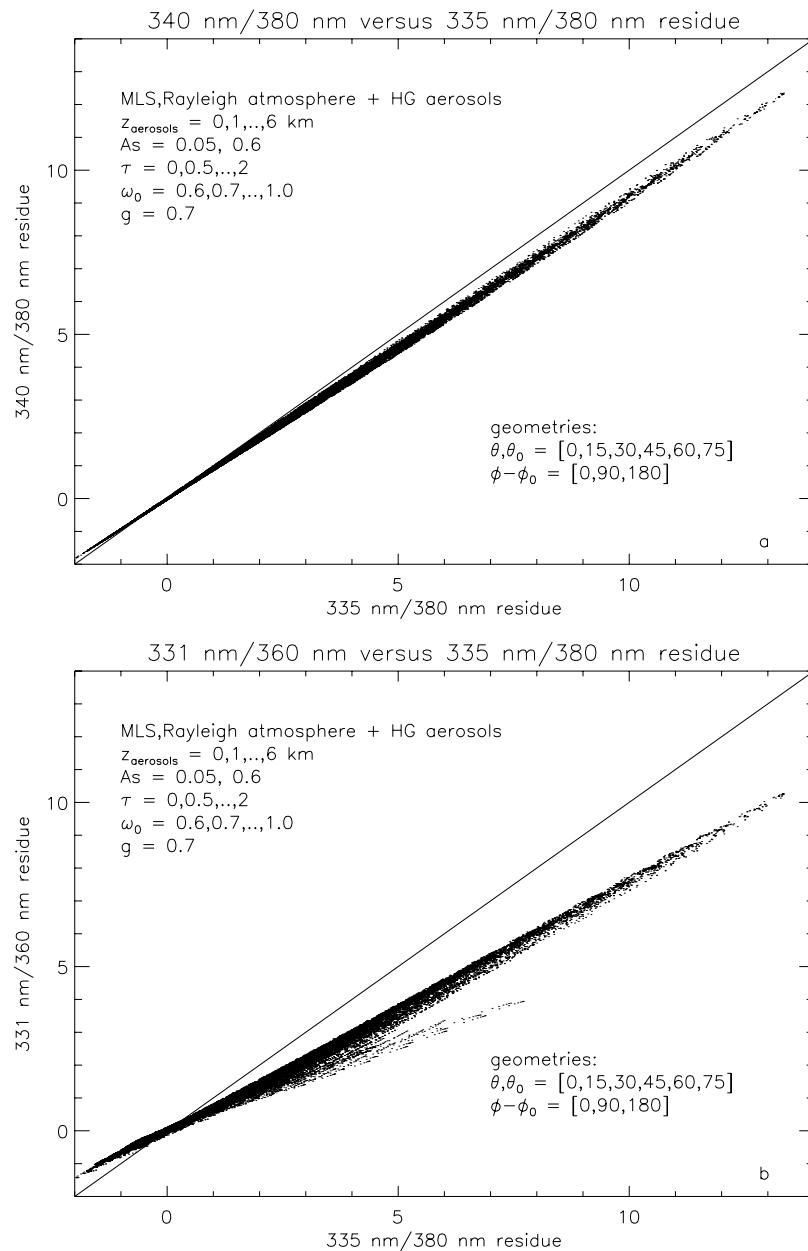


**Figure 8.** (a) Scatterplot of residues calculated for  $\lambda = 340$  nm versus  $\lambda = 335$  nm ( $\lambda_0 = 380$  nm in both cases). (b) Scatterplot of residues calculated for  $\lambda = 331$  nm and  $\lambda_0 = 360$  nm versus residues calculated for  $\lambda = 335$  nm and  $\lambda_0 = 380$  nm. Residues are determined at all geometries with  $\theta_0$  and  $\theta = [0^\circ, 15^\circ, 30^\circ, 45^\circ, 60^\circ, \text{ and } 75^\circ]$ ,  $\phi - \phi_0 = [0^\circ, 90^\circ, \text{ and } 180^\circ]$ . A 1 km thick aerosol layer was present between 0 and 6 km, in steps of 1 km, the aerosol optical thickness was varied between 0 and 2, in steps of 0.2, the single scattering albedo of the aerosol was varied between 0.6 and 1, in steps of 0.1. The surface albedo was 0.05 or 0.6.

was launched in July 1996 into a Sun-synchronous orbit with an altitude of 500 km and an equator crossing time of about 1116 LT to provide supplemental measurements, but was boosted to a higher orbit (740 km altitude) to replace the failed ADEOS/TOMS in December 1997. The new orbit resulted in 90% daily coverage (84% at equator and 100% at latitudes  $\geq 30^\circ$ ).

[59] The TOMS instruments measure incident solar radiation and backscattered UV radiation at six discrete one nm wide wavelength bands. For the first three TOMS instru-

ments these wavelength bands were centered around 313, 318, 331, 340, 360 and 380 nm. On EP/TOMS the 340 and 380 bands have been eliminated in favor of a 309 nm and a 322 nm band (Table 2). As a result, the AAI from EP/TOMS was calculated with the 331 nm/360 nm pair, while previous AAI were based on the 340 nm/380 nm pair.

[60] TOMS daily residues and TOMS monthly AAI can be downloaded from the Internet, both gridded to  $1^\circ$  latitude  $\times$   $1.25^\circ$  longitude grid boxes. TOMS AAI are calculated by averaging daily positive residues over one

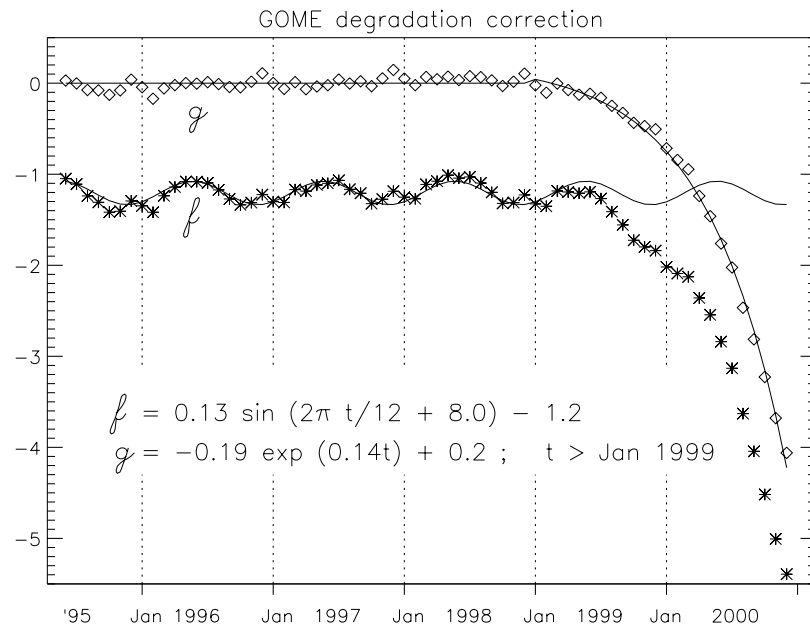


**Figure 9.** Diagram illustrating the GOME degradation correction. The asterisks denote the global monthly mean AAI for the period 1995–2000. The period 1995–1998 was fitted to a sine function with a period of one year  $f = a_0 \sin(2\pi t/12 + a_1) + a_2$ , with  $a_0 = 0.13$ ,  $a_1 = 8.0$ ,  $a_2 = -1.2$ . The difference between the sine and AAIs of the last two months was fitted to an exponential function  $g = a_0 \exp(a_1 t) + a_2$ , with  $a_0 = -0.19$ ,  $a_1 = 0.14$ ,  $a_2 = 0.2$ .

month, with all averages lower than 0.7 set to zero. Erroneous measurements are flagged, which is true at least for all measurements at latitudes higher than  $60^\circ\text{N}$  and  $60^\circ\text{S}$ , where satellite measurements are inaccurate due to large solar zenith angles.

#### 4.2. GOME

[61] GOME is a 4-channel grating spectrometer, operating in the wavelength range of 237–794 nm with a spectral resolution of 0.2–0.4 nm. GOME was launched in April 1995 on board the ERS-2 satellite into a near-polar Sun-synchronous orbit at a mean altitude of about 785 km, with a mean local equator crossing time of 1030 LT. GOME performs nadir observations by scanning the surface from east to west (corresponding to a viewing zenith angle of  $-30^\circ$  to  $+30^\circ$ ) in 4.5 s. One across-track scan is divided into three 1.5 s ground pixels with an average size of  $40 \times 320 \text{ km}^2$  each. For about 10% of the time, the swath is reduced to 240 km, and all pixel sizes are four times smaller. Once per day the Sun is observed over a diffuser plate for radiometric calibration. A region over the Himalayas is never observed, because in this region data from the ERS-2 satellite is downlinked to Earth and during this time no observation can be stored. Since 1999–2000 GOME suffers from serious radiometric degradation. Only GOME data from 27 June 1995 to 31 December 2000 were used.

#### 4.3. Data Preparation and Corrections

[62] A residue  $r$  was determined for each pair of calibrated GOME TOA reflectances centered at 335 nm and 380 nm, averaged over a one nm wide wavelength window (see Koелеmeijer *et al.* [2003] for more details on the data

calibration). The ground pressure in the residue calculation was found from the ETOPO-5 surface elevation database [Haxby *et al.*, 1983], assuming the MLS profile. For ozone the GOME level 2 total ozone column product was used. The solar and viewing angles were averaged over the GOME ground pixels. Pixels with solar zenith angles larger than  $80^\circ$  were discarded. The residues were gridded into  $1^\circ$  latitude  $\times$   $1.25^\circ$  longitude boxes for each day.

[63] Daily and monthly mean AAIs were determined by averaging all positive residues in a box. To avoid single aerosol events from showing up in the monthly mean plots, a minimum of two AAIs was set for the monthly average to be valid. This excluded 0.01% of the points. AAI values greater than 5.5 (0.0017% of the data) were considered outliers and removed. At latitudes higher than  $60^\circ\text{N}$  and  $60^\circ\text{S}$  the AAI was not retrieved. Note that TOMS monthly mean AAIs start at 0.7 and GOME monthly mean AAIs start at 0.0.

[64] As mentioned, GOME suffered from severe degradation from 1999 onwards. The residues clearly show this degradation. The yearly averaged residue over 1996–1998 was very constant around  $-1$ , while after 1998 it decreased rapidly to  $-2$  in 1999 and even  $-3.5$  in 2000. To correct for this degradation the global monthly averaged residue was analyzed. As shown in Figure 9, the residue varies sinusoidally over the years from 1995 to 1998, after that the signal decreases rapidly. The variation found in 1995–1998 was fitted to a sine with a period of one year. An amplitude of 0.13 and a phase shift of 8.0 (months) was found, the mean residue was  $-1.2$ . The residues from the years 1999 and 2000 were corrected with the difference between the global monthly averaged residues and the fit. This difference increases exponentially. The last two months of 2000 the

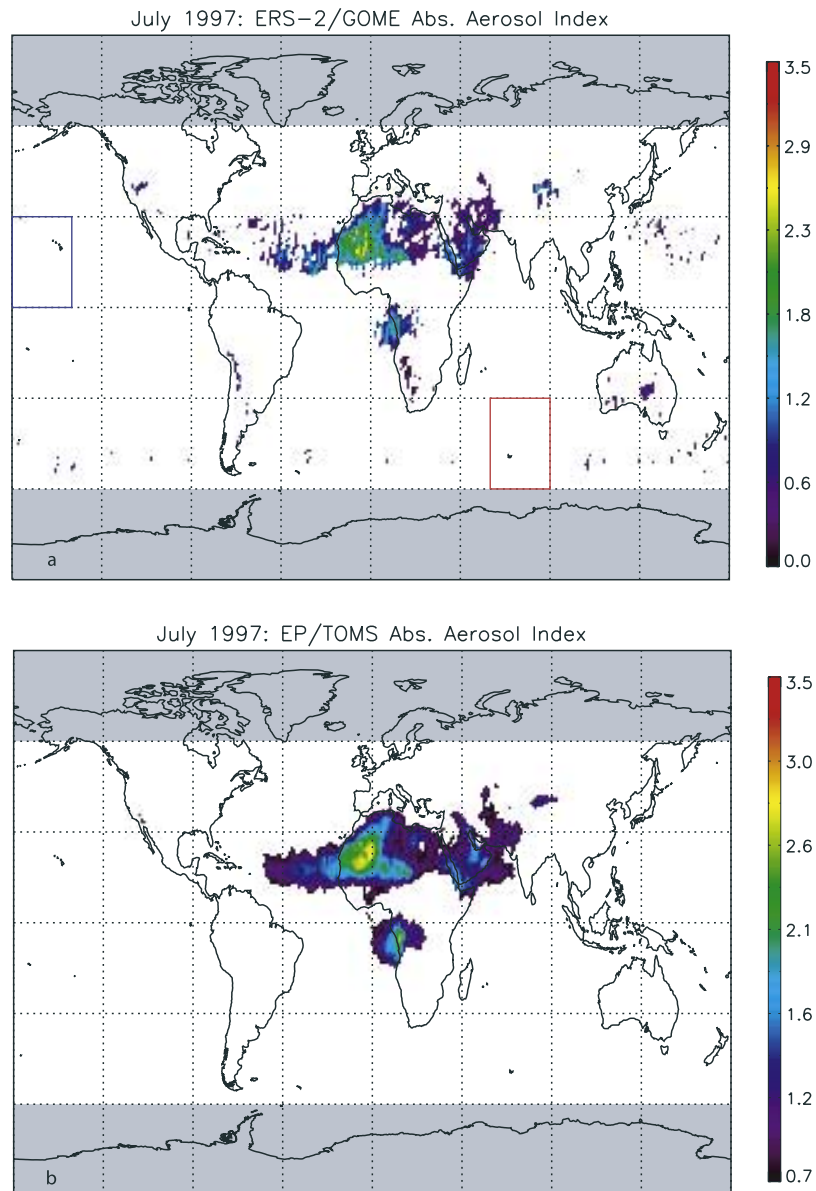


**Figure 10.** (a) Global map of the monthly mean GOME AAI for July 1997. (b) Same for TOMS for July 1997. In the shaded areas, no indices are retrieved. The blue and the red boxes in Figure 10a indicate the areas for the solar zenith angle error analysis (see text).

residues and AAIs are not reliable anymore, because the correction is too large.

[65] The sinusoidal variation was investigated further. To exclude the possibility of a solar zenith angle  $\theta_0$  error, the monthly averaged residue was determined in two  $30^\circ \times 30^\circ$  areas, one on the northern hemisphere (NH) containing Hawaii ( $0^\circ$ – $30^\circ$  N,  $150^\circ$ – $180^\circ$  W, blue box in Figure 10a) and one on the southern hemisphere (SH) over the southern Indian Ocean ( $30^\circ$ – $60^\circ$  S,  $60^\circ$ – $90^\circ$  E, red box in Figure 10a). In these areas very few aerosols are found throughout the year. In both areas a sinusoidal variation was found, but the phase shift was almost the same in both the NH (7.6 months) and the SH (7.9 months). As the  $\theta_0$  variations over both boxes have opposite signs, so would the residue variations if they were caused by  $\theta_0$  errors.

[66] A possible explanation of the sinusoidal variation is the GOME solar calibration which is performed daily. The angle under which the Sun illuminates the diffuser varies throughout the year. An error in the characterization of the Bi-directional Scattering Distribution Function (BSDF) of the diffuser could lead to an error in the reflectance.

[67] The data are available at <http://www.temis.nl>. Both the daily files with the gridded residues and the monthly mean AAI and pictures of global monthly mean AAI can be found there.

[68] Figure 10a is an example of the monthly averaged GOME 335 nm/380 nm AAI for May 1998. The TOMS index is shown in Figure 10b for the same month. The GOME AAI compares very well with the TOMS AAI. TOMS uses a threshold of 0.7, i.e., positive residues are

averaged, but only averages larger than 0.7 are plotted. For GOME another threshold applies, because GOME data are calibrated differently and GOME uses different residue wavelengths than TOMS, so the absolute values also differ.

[69] The GOME AAI is more patchy than the TOMS index. This is because GOME covers the Earth only every three days, while TOMS has daily global coverage, so GOME has three times less data.

[70] To indicate the coverage of GOME an extra data file is provided on the Internet for every month of data available. This data file gives the number of residue values per bin in that month. An example of this number of values is given in Figure 11c. This figure shows the region centered on the Himalayas, which is the region where ERS-2 data are downlinked to the Earth and no data storage is possible, resulting in a gap where no data are ever available and a boundary area where only very few observations are available. The result of this phenomenon can be seen in Figures 11a and 11b. The TOMS data (Figure 11b) clearly shows an aerosol plume over India, which is absent in the GOME data (Figure 11a). This can be observed almost every spring, when TOMS data show aerosol plumes in this area, contrary to GOME data. Please recall that GOME needs at least two values per month in one bin to produce a valid monthly mean.

[71] The GOME data show dense and persistent aerosol plumes over North Africa for all seasons, connected to very frequent dust storms over this part of the African continent, see Figure 12; in these figures the seasonal averages over all years are plotted. The center of this plume is over the Sahara during the boreal summer and shifts to the south during the boreal winter. This feature, and other structures over the large aerosol sources, correspond well with those found in the TOMS data.

[72] From July to August a persistent plume is present west of Angola. This is biomass burning aerosol from forest fires.

[73] In all seasons plumes are present over Asia. The plumes in middle east Asia may be dust aerosols from the Gobi desert, but they are generally not present in the TOMS data. A small part of the signal may be due to the presence of the Himalayas, which are not well resolved in the ETOPO-5 topography database. The database has a spatial resolution of  $12' \times 12'$ , which might be insufficient to resolve the high peaks of the Himalayas. This introduces errors in the ground pressure values, yielding high apparent residues (Figure 4a). The latter argument also holds for the signal over the Andes; a small but very persistent signal can be found there, which is probably caused by the insufficient resolution of the topography database. An Amazonian aerosol plume can be found occasionally, connected to biomass burning of the tropical forests.

[74] Over the southern oceans around Antarctica some spots of AAI can be found during spring and summer (Figure 12), which are absent in the TOMS data (compare Figures 10a and 10b). The reason for these AAIs is unclear, but they might be caused by errors due to high solar zenith angles.

[75] As another example of the GOME AAI the Indonesian wildfires of September to November 1997 are considered. These are captured very well by GOME (Figure 13). These fires released large amounts of UV absorbing aero-

sols, which show up in the data as high AAI values. The maxima of the 3 months averaged AAI correspond very well with the maxima of the total number of ATSR-2 fire-counts [Duncan *et al.*, 2003, Figure 1].

[76] To determine the zonal behavior of the AAI, the monthly means of the AAI were averaged over longitude per year from July 1995 until December 2000 (Figure 14, solid line). A clear maximum in the AAI exists over the subtropics in the NH, caused by the persistent subtropical aerosol sources like the Sahara and Gobi deserts. In the SH a smaller peak can be found in the subtropics, mainly caused by forest fires in the tropical forests and dust from Australian deserts. However, this peak is not always clear and shifts between  $45^\circ\text{S}$  and the equator. Between  $45^\circ\text{S}$  and  $60^\circ\text{S}$  another local maximum can be found which grows continuously from year to year. In 1995 the peak is almost absent, while in 1999 and 2000 its amplitude is bigger than that of the southern subtropical peak (see Figure 14). The reason for these high values of the AAI is unclear, but is probably a calibration error.

[77] The NH subtropical maximum in the zonally averaged GOME AAI is very stable from year to year at about 0.15, contrary to the zonally averaged TOMS AAI, which was determined from July 1996 to December 2000 (Figure 14, dashed line). The TOMS AAI has its maximum at the same latitude as the GOME AAI, but its amplitude is always higher than that of the GOME AAI, and it is much more variable, ranging from 0.20 to 0.32. As the TOMS AAI was determined with the 331 nm/360 nm pair it would be expected to be about 35% lower than the GOME AAI, but instead it is up to twice as high. This might be caused by the lower sampling rate of GOME. As the AAI is an average of only positive residues (section 4.2) single high values can show up in these averages, and TOMS has a three times higher chance of sampling such a high value than GOME. Furthermore, the TOMS pixel size of  $50 \times 50$  km is much smaller than the GOME pixel size of  $40 \times 320$  km, which raises the chance of high residue values.

## 5. Conclusion

[78] The Absorbing Aerosol Index (AAI) separates absorbing from scattering effects in the UV, which makes it useful to monitor UV-absorbing aerosols like desert dust and biomass burning aerosols from space, both over land and sea. The AAI is based on the spectral contrast of the reflectances at two UV wavelengths, compared to that of a pure Rayleigh atmosphere. Its absolute value depends on many parameters, most notably aerosol optical thickness, the height of the absorbing layer, and in the case of aerosols, the microphysical properties of the aerosols. This makes a unique retrieval of one of these aerosol quantities from the AAI difficult.

[79] Data from the Global Ozone Monitoring Experiment (GOME) instrument can be used to retrieve the AAI. These AAI data correspond well with known UV-absorbing aerosol events and the TOMS AAI. As GOME has a global coverage only every three days, the AAI is not very suitable to monitor aerosol events on a day-to-day basis, but is well suited to provide monthly global maps of absorbing aerosols. The GOME AAI is particularly useful in the period

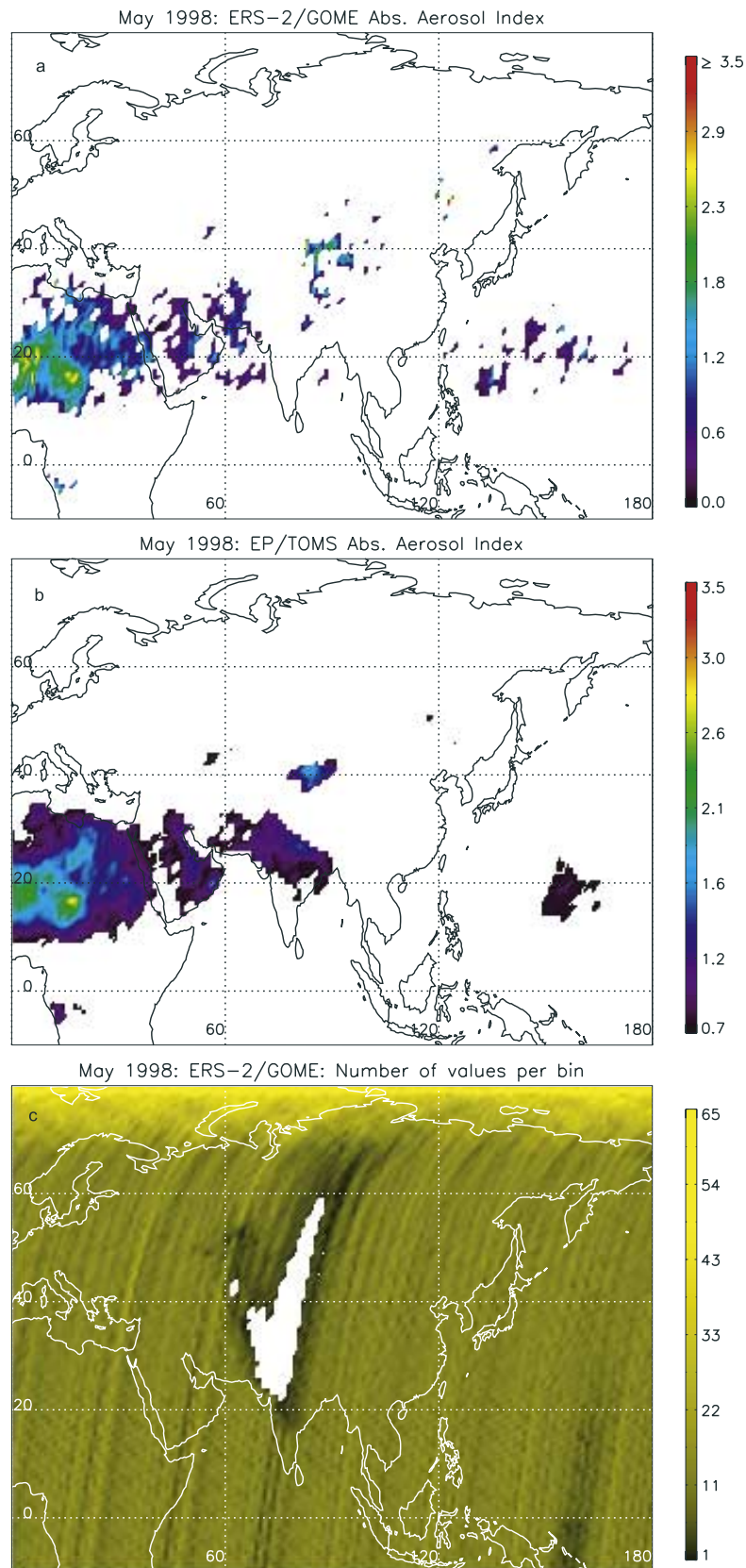


**Figure 11.** (a) Monthly mean GOME AAI in May 1998 for the region centered on the Himalayas. (b) Same for TOMS in May 1998. (c) Plot of the number of residues used per bin to calculate the monthly mean GOME AAI in May 1998 for the same region as Figures 11a and 11b. The number of values is low (black) and even zero for a large part (white), due to GOME's data storage problem during downlinking of data.

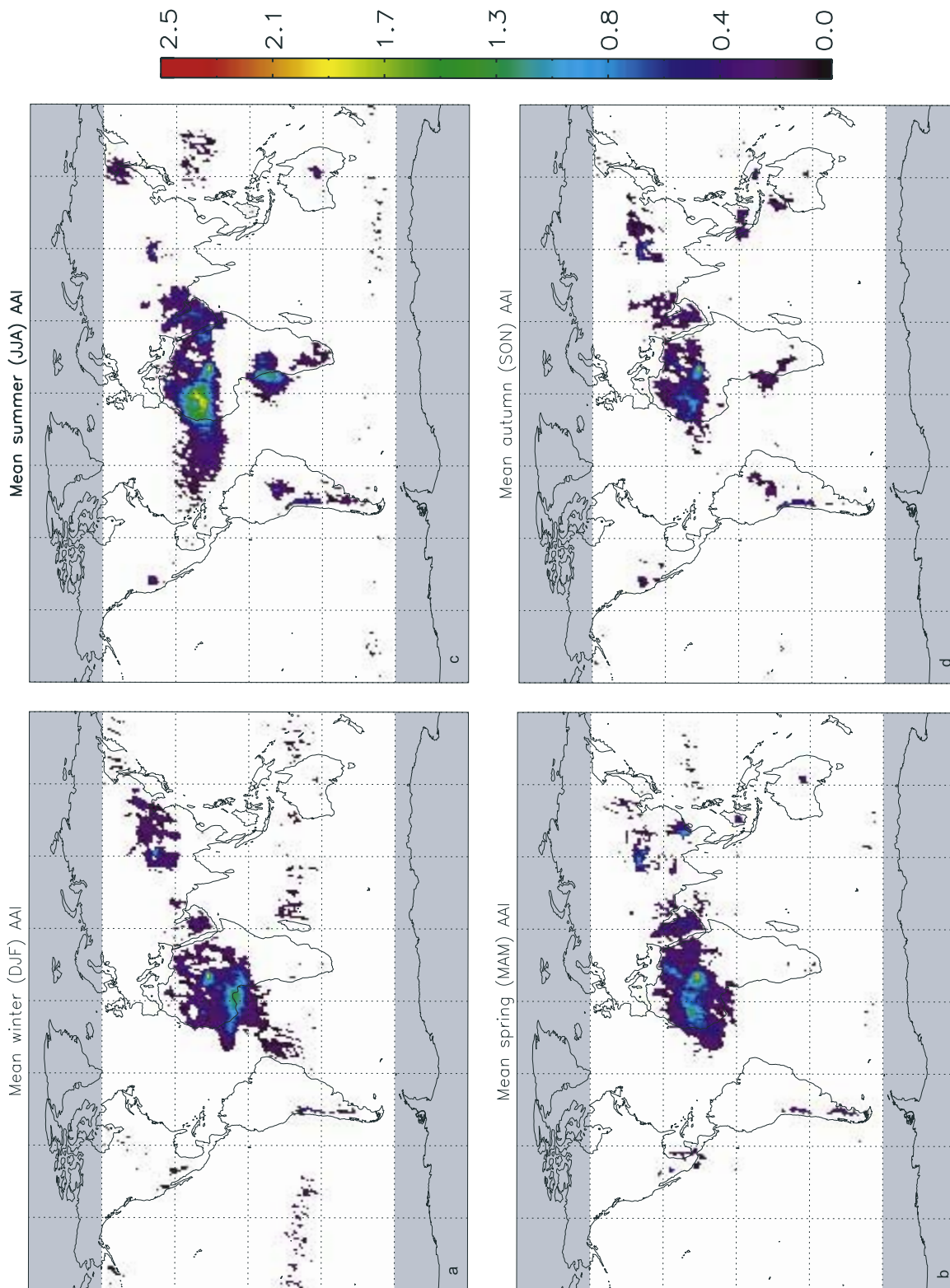


**Figure 12.** Global maps of the GOME AAI for different seasons during the 5.5-year period June 1995 to December 2000. (a) Average AAI in December, January, and February (DJF) of all years. (b) Same as Figure 12a for March, April, and May. (c) Same as Figure 12a for June, July, and August. (d) Same as Figure 12a for September, October, and November.

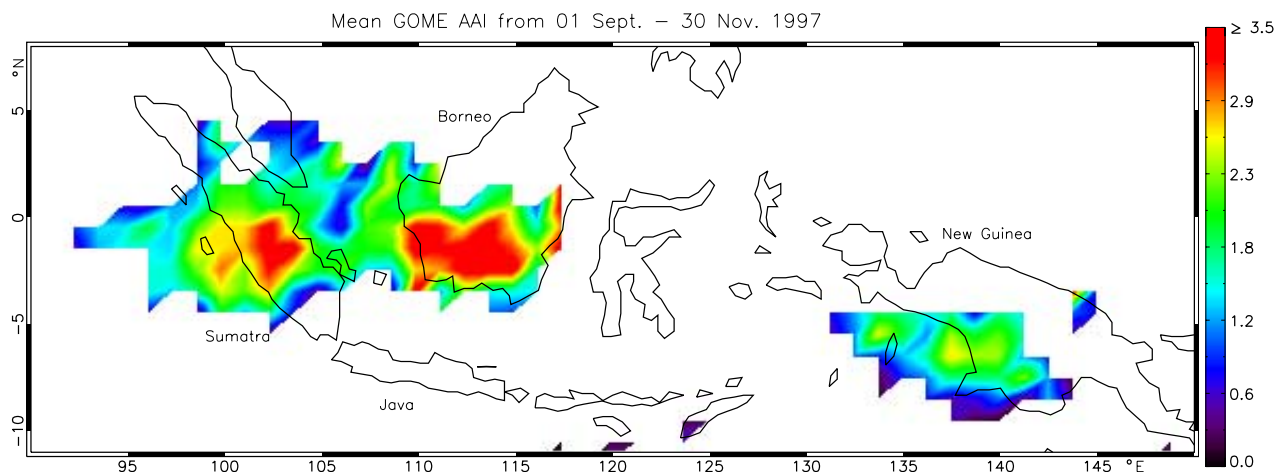


**Figure 13.** Indonesian wildfires in the fall of 1997. Shown is the AAI averaged from 1 September to 30 November 1997.

July 1995 to August 1996, when there were no measurements from TOMS.

[80] The residue  $r$  is very sensitive to errors in the reflectances and can be used as an additional calibration

tool. The sinusoidal variation found in the global AAI data is probably due to a calibration error previously undetected in the GOME radiance data. The amplitude of the variation was 0.15 in  $r$ , which corresponds in first order approxima-

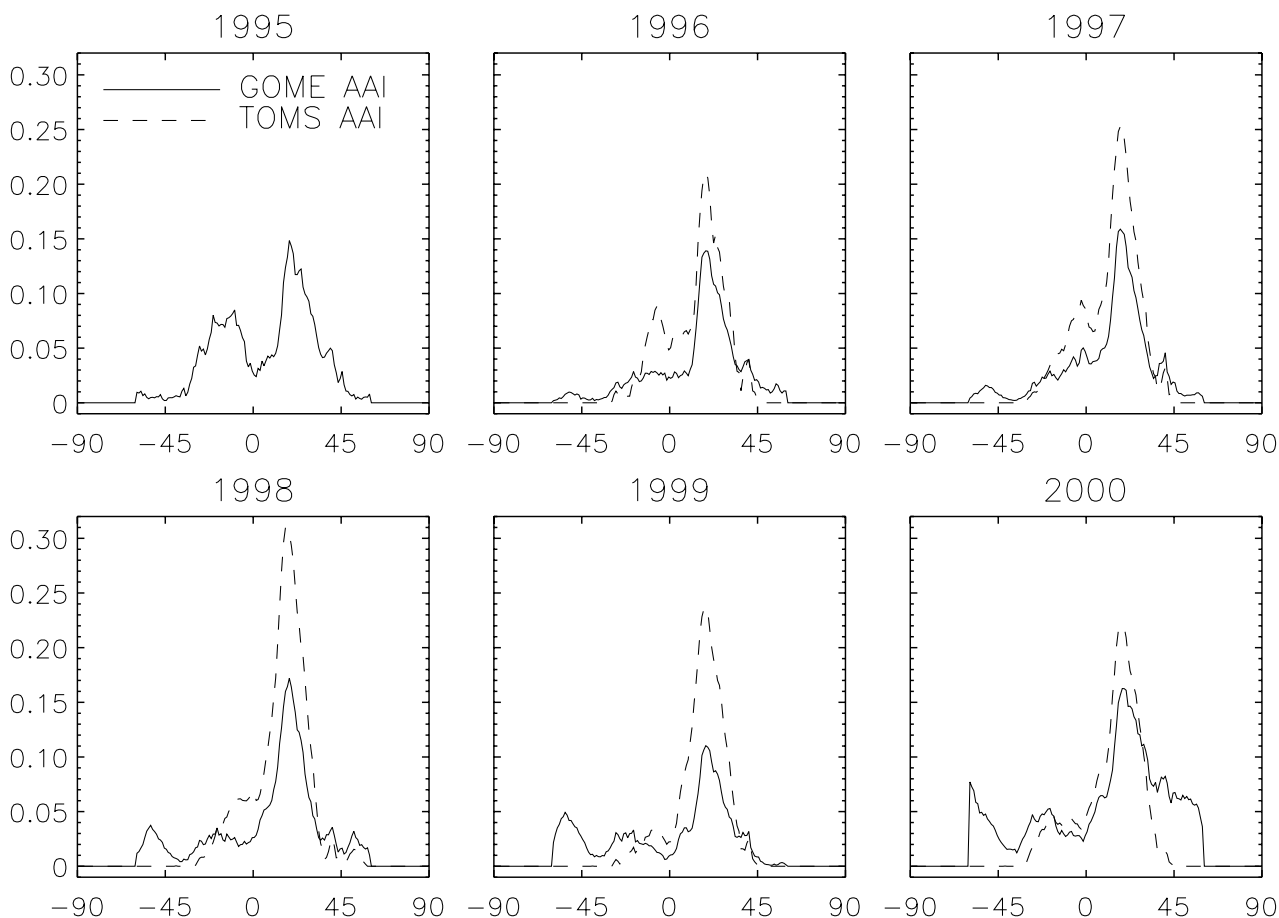


**Figure 14.** Zonal mean of GOME AAI (solid line) and the TOMS AAI (dashed line) for six consecutive years as a function of latitude. Negative latitudes are on the southern hemisphere. From GOME only data from July to December were available in 1995, and in 2000 the last two months were discarded. TOMS data were available from July 1996 to December 2000.

tion to a very small variation in  $R_{\lambda}^{meas}$  of 0.0035 (see equation (4)).

[81] The cause for the AAI over the southern oceans around Antarctica is unclear. Applying the calibration correction described previously slightly reduced the signal, but did not eliminate it. It is unlikely that these AAIs correspond to aerosol events in this area, because the air around Antarctica is usually very clean and also the TOMS data do not show any high values there. However, no explanation was found so far.

[82] The topography database used for retrieval of the GOME AAI has an insufficient spatial resolution to resolve the steepest mountain ranges in the world, like the Himalayas and the Andes. This yields apparent residues over mountainous areas when there are no aerosol events. This problem can be resolved with a database with a higher resolution.

[83] The quantitative use of the aerosol information content in the satellite measurements of near UV radiances has been used to develop an algorithm to retrieve aerosol optical thickness and single scattering albedo [Torres et al., 1998, 2002]. The near UV algorithm has been applied to the TOMS record (1979–2000), to produce the longest available AOT data set over the oceans and the continents [Torres et al., 2002]. Both the AOT and the single scattering albedo products have been validated making use of ground-based observations [Torres et al., 2002, 2005]. The near UV algorithm is also being applied to observations by the recently deployed Ozone Monitoring Instrument (OMI) on the Aura satellite.

[84] This work could be extended with SCIAMACHY data, once data will become available. The GOME and SCIAMACHY extended spectral range may be used to improve the AAI. Incorporating information at other wavelengths, e.g., in the visible, may help separate different aerosol species or retrieve other aerosol information [Torres et al., 2001].

[85] **Acknowledgment.** This work was financed by the Netherlands Agency for Aerospace Programmes (NIVR) SCIAMACHY validation project and DAEDALUS, project EVK2-CT-2002-00174.

## References

- Alpert, P., and E. Ganor (2001), Sahara mineral dust measurements from TOMS: Comparison to surface observations over the Middle East for the extreme dust storm, March 14–17, 1998, *J. Geophys. Res.*, *106*(D16), 18,275–18,286.
- Anderson, G. P., S. A. Clough, F. X. Kneizys, J. H. Chetwynd, and E. P. Shettle (1986), AFGL atmospheric constituent profiles, *Tech. Rep. AFGL-TR-86-0110*, Air Force Geophys. Lab., Bedford, Mass.
- Chandrasekhar, S. (1960), *Radiative Transfer*, 393 pp., Dover, Mineola, N. Y.
- Chiapello, I., J. M. Prospero, J. R. Herman, and N. C. Hsu (1999), Detection of mineral dust over the North Atlantic Ocean and Africa with the Nimbus 7 TOMS, *J. Geophys. Res.*, *104*(D8), 9277–9291.
- De Haan, J. F., P. B. Bosma, and J. W. Hovenier (1987), The adding method for multiple scattering calculations of polarized light, *Astron. Astrophys.*, *183*, 371–391.
- Dubovik, O., B. Holben, T. F. Eck, A. Smirnov, Y. J. Kaufman, M. D. King, D. Tanré, and I. Slutsker (2002), Variability of absorption and optical properties of key aerosol types observed in worldwide locations, *J. Atmos. Sci.*, *59*, 590–608.
- Duncan, B. N., I. Bey, M. Chin, L. J. Mickley, T. D. Fairlie, and R. V. Martin (2003), Indonesian wildfires of 1997: Impact on tropospheric chemistry, *J. Geophys. Res.*, *108*(D15), 4458, doi:10.1029/2002JD003195.
- Gleason, J. F., N. C. Hsu, and O. Torres (1998), Biomass burning smoke measured using backscattered ultraviolet radiation: SCAR-B and Brazilian smoke interannual variability, *J. Geophys. Res.*, *103*(D24), 31,969–31,978.
- Haxby, W. F., J. L. L. G. D. Karner, and J. K. Weisell (1983), Digital images of combined oceanic and continental data sets and their use in tectonic studies, *Eos. Trans. AGU*, *64*, 995–1004.
- Heney, L. G., and J. L. Greenstein (1941), Diffuse radiation in the galaxy, *Astrophys. J.*, *93*, 70–83.
- Herman, J. R., P. K. Bhartia, O. Torres, C. Hsu, C. Seftor, and E. A. Celarier (1997), Global distributions of UV-absorbing aerosols from NIMBUS 7/TOMS data, *J. Geophys. Res.*, *102*(D14), 16,911–16,922.
- Hsu, N. C., J. R. Herman, P. K. Bhartia, C. J. Seftor, O. Torres, A. M. Thompson, J. F. Gleason, T. Y. F. Eck, and B. N. Holben (1996), Detection of biomass burning smoke from TOMS measurements, *Geophys. Res. Lett.*, *23*(7), 745–748.
- Hsu, N. C., J. R. Herman, J. F. Gleason, O. Torres, and C. J. Seftor (1999), Satellite detection of smoke aerosols over a snow/ice surface by TOMS, *Geophys. Res. Lett.*, *26*(8), 1165–1168.
- Intergovernmental Panel on Climate Change (IPCC) (2001), *Working Group I to the Third Assessment Report of the Intergovernmental Panel on Climate Change*, 295 pp., Cambridge Univ. Press, New York.
- Koelemeijer, R. B. A., J. F. de Haan, and P. Stammes (2003), A database of spectral surface reflectivity in the range 335–772 nm derived from 5.5 years of GOME observations, *J. Geophys. Res.*, *108*(D2), 4070, doi:10.1029/2002JD002429.
- Mahowald, N. M., and J.-L. Dufresne (2004), Sensitivity of TOMS aerosol aerosol index to boundary layer height: Implications for detection of mineral aerosol sources, *Geophys. Res. Lett.*, *31*, L03103, doi:10.1029/2003GL018865.
- Moulin, C., and I. Chiapello (2004), Evidence of the control of summer atmospheric transport of African dust over the Atlantic by Sahel sources from TOMS satellites (1979–2000), *Geophys. Res. Lett.*, *31*, L02107, doi:10.1029/2003GL018931.
- Pandithurai, G., R. T. Pinker, O. Dubovik, and T. O. Aro (2001), Remote sensing of aerosol optical characteristics in sub-Sahel, West Africa, *J. Geophys. Res.*, *106*(D22), 28,347–28,356.
- Patterson, E. M., D. A. Gillete, and B. H. Stockton (1977), Complex index of refraction between 300 and 700 nm for Saharan aerosol, *J. Geophys. Res.*, *82*, 3153–3160.
- Seftor, C. J., N. C. Hsu, J. R. Herman, P. K. Bhartia, O. Torres, W. I. Rose, D. J. Schneider, and N. Krotkov (1997), Detection of volcanic ash clouds from Nimbus 7/total ozone mapping spectrometer, *J. Geophys. Res.*, *102*(D14), 16,749–16,759.
- Sinyuk, A., O. Torres, and O. Dubovik (2003), Combined use of satellite and surface observations to infer the imaginary part of the refractive index of Saharan dust, *Geophys. Res. Lett.*, *30*(D2), 1081, doi:10.1029/2002GL016189.
- Stammes, P. (2001), Spectral radiance modelling in the UV-visible range, in *IRS 2000: Current Problems in Atmospheric Radiation*, edited by W. Smith and Y. Timofeyev, pp. 385–388, A. Deepak, Hampton, Va.
- Torres, O., and P. K. Bhartia (1999), Impact of tropospheric aerosol absorption on ozone retrieval from backscattered ultraviolet measurements, *J. Geophys. Res.*, *104*(D17), 21,569–21,577.
- Torres, O., P. K. Bhartia, J. R. Herman, Z. Ahmad, and J. Gleason (1998), Derivation of aerosol properties from satellite measurements of backscattered ultraviolet radiation: Theoretical basis, *J. Geophys. Res.*, *103*(D14), 17,099–17,110.
- Torres, O., R. Decae, P. Veeckind, and G. de Leeuw (2001), OMI Aerosol Retrieval Algorithm, in *OMI-EOS Algorithm Theoretical Basis Document*, chap. 4, pp. 1–24, R. Neth. Meteorol. Inst., De Bilt, Netherlands.
- Torres, O., P. K. Bhartia, J. R. Herman, A. Sinyuk, P. Ginoux, and B. Holben (2002), A long-term record of aerosol optical depth from TOMS observations and comparison to AERONET measurements, *J. Atmos. Sci.*, *59*(3), 398–413.
- Torres, O., P. K. Bhartia, A. Sinyuk, and E. Welton (2005), TOMS measurements of aerosol absorption from space: Comparison to SAFARI 2000 ground-based observations, *J. Geophys. Res.*, doi:10.1029/2004JD004611, in press.
- Torricella, F., E. Cattani, M. Cervino, R. Guzzi, and C. Levoni (1999), Retrieval of aerosol properties over the ocean using Global Ozone Monitoring Experiment measurements: Method and applications to test cases, *J. Geophys. Res.*, *104*(D10), 12,085–12,098.

M. de Graaf and P. Stammes, Royal Netherlands Meteorological Institute, Wilhelminalaan 30, 3732 GK De Bilt, Netherlands. (graafdem@knmi.nl; stammes@knmi.nl)

R. B. A. Koelemeijer, Netherlands Environmental Assessment Agency, National Institute of Public Health and the Environment, P.O. Box 1, 3720 BA Bilthoven, Netherlands. (robert.koelemeijer@rivm.nl)

O. Torres, NASA Goddard Space Flight Center, Code 916, Greenbelt, MD 20771, USA. (torres@tparty.gsfc.nasa.gov)